METRICA
METRology Institutional CAtalog

ISTITUTO NAZIONALE DI RICERCA METROLOGICA
Repository Istituzionale

Confinement-induced physicochemical and optical modulation of metalloporphyrins within mesoporous silica MCM-41

Original
Confinement-induced physicochemical and optical modulation of metalloporphyrins within mesoporous silica MCM-41 / Lihitkar, P.B., Kale, S., Afre, R.A., Pugliese, D.. - In: MATERIALS SCIENCE AND ENGINEERING B-SOLID STATE MATERIALS FOR ADVANCED TECHNOLOGY. - ISSN 0921-5107. - 335:(2027). [10.1016/j.mseb.2026.119966]

Availability:
This version is available at: 11696/90639 since: 2026-11-02T07:10:12Z

Publisher:
Elsevier Ltd

Published
DOI:10.1016/j.mseb.2026.119966

Terms of use:

This article is made available under terms and conditions as specified in the corresponding bibliographic description in the repository

Publisher copyright

(Article begins on next page)

27 November 2026

Materials Science and Engineering B 335 (2027) 119966

Contents lists available at ScienceDirect

Materials Science & Engineering B

journal homepage: www.elsevier.com/locate/mseb

Confinement-induced physicochemical and optical modulation of metalloporphyrins within mesoporous silica MCM-41

Prashant B. Lihitkar [a], Sonali Kale [b], Rakesh A. Afre [c,d,*], Diego Pugliese [e,*]

[a] Department of Chemistry, Lokmanya Tilak Mahavidyalaya, Wani, Yavatmal, Maharashtra, 445304, India
[b] Department of Applied Sciences and Humanities, Pimpri Chinchwad College of Engineering, Nigdi, Pune, Maharashtra, 411004, India
[c] School of Technology and Research, Dnyaan Prasad Global University, Sant Tukaram Nagar, Pimpri, Pune, Maharashtra, 411018, India
[d] Department of Physics, Dr. D. Y. Patil Institute of Technology, Sant Tukaram Nagar, Pimpri, Pune, Maharashtra, 411018, India
[e] Division of Applied Metrology and Engineering, National Institute of Metrological Research (INRiM), Torino, 10135, Italy

ARTICLE INFO

Keywords:
Metalloporphyrins
Mesoporous silica MCM-41
Optical properties
Fluorescence spectroscopy
Host–guest interactions

ABSTRACT

Amino-functionalized mesoporous silica MCM-41 was used as a confined host for free-base tetraphenylporphyrin (TPP) and Zn-, Co-, and Fe-tetraphenylporphyrins (M-TPP). The composites were prepared by impregnation and characterized using X-ray diffraction (XRD), nitrogen (N_2) adsorption–desorption, diffuse-reflectance ultraviolet–visible (UV–Vis) spectroscopy, photoluminescence (PL) spectroscopy, Fourier transform infrared (FTIR) spectroscopy, and time-resolved fluorescence spectroscopy. The ordered MCM-41 structure was retained after functionalization and porphyrin incorporation, while the Brunauer–Emmett–Teller (BET) surface area decreased from 947 m^2/g for Si-MCM-41 to 47–67 m^2/g for the porphyrin-containing composites. Diffuse-reflectance UV–Vis measurements showed Soret-band red shifts of 16 and 24 nm for ZnTPP-M and CoTPP-M, respectively, together with red shifts of the Q bands. PL measurements revealed emission blue shifts of 15 nm for TPP and 19 nm for FeTPP after incorporation. The observed spectral changes are attributed to the combined effects of the local silica environment, host–guest interactions, confinement, and possible porphyrin aggregation. FTIR spectroscopy revealed changes in the chemical environment of the aminopropyl-functionalized silica after porphyrin incorporation, although the available data do not independently establish specific metal–nitrogen coordination. Multiexponential fluorescence decay profiles indicated heterogeneous excited-state environments within the composites. Overall, the results demonstrate that amino-functionalized MCM-41 modifies the physicochemical and photophysical behavior of incorporated porphyrins and provide a basis for the future development of supported porphyrin materials for optical sensing and photocatalytic applications.

1. Introduction

Metalloporphyrins are widely used as catalysts in homogeneous oxidation reactions [1–4]. However, difficulties arise in separating the catalyst in homogeneous systems. The incorporation of metalloporphyrins onto a solid support such as mesoporous silica MCM-41 represents an effective strategy for shifting liquid-phase oxidation processes from homogeneous to heterogeneous systems [5]. Furthermore, metalloporphyrins supported on porous solid supports possess physically separated active sites, thereby reducing catalyst self-destruction and aggregation [6].

Biological molecules such as enzymes [7], α-amylase [8], and vitamin B_{12} [9] have been immobilized within functionalized mesoporous silica MCM-41. Such organic–inorganic composites have been demonstrated to be effective catalysts in oxidation reactions [9]. Mesoporous materials exhibit unique properties that are highly desirable for adsorption applications, including uniform pore sizes and high surface area, thereby enabling efficient separation based on size exclusion and tailored surface chemistry [10]. Mesoporous materials such as MCM-41 and MCM-48 are widely used as molecular sieves for the separation of biological molecules, including proteins (lysozyme and trypsin) and vitamins (e.g., riboflavin) [11].

Mesoporous silicate species of the type MCM-41 provide large pore volume, narrow pore size distributions in the nanometer range, and extremely high surface area [1,2,12]. The porphyrin aggregates formed within the pores of MCM-41 are shown to assemble via J-aggregation of

* Corresponding authors.
E-mail addresses: rakesh.afre@dypdpu.edu.in (R.A. Afre), d.pugliese@inrim.it (D. Pugliese).

https://doi.org/10.1016/j.mseb.2026.119966
Received 13 May 2026; Received in revised form 10 October 2026; Accepted 26 October 2026
Available online 28 October 2026
0921-5107/© 2026 The Author(s). Published by Elsevier B.V. This is an open access article under the CC BY license (http://creativecommons.org/licenses/by/4.0/).

the molecules. The composite structure can be regarded as a "ship-in-a-bottle" type nanomaterial [13]. The resulting properties of these composites exhibit quantum confinement effects. Moreover, the self-assembly of porphyrin aggregates without the formation of covalent linkages is of considerable scientific interest [14]. Such aggregates are composite structures in which optically induced transient structural changes influence photon dynamics, playing an important role in photosynthesis-related processes [15–17].

The photoionization of metalloporphyrins in porous inorganic solids such as zeolites [18,19] and silica gels [20] has been extensively studied. Due to steric and electrostatic effects, these materials provide an appropriate microenvironment that retards back electron transfer and increases the lifetime of photo-generated radical ions. However, the use of zeolites presents limitations, as they can oxidize aromatic molecules to their corresponding cation radicals by electron acceptance. In addition, the diameter of the supercages of zeolites X and Y is approximately 13 Å, with cage openings of about 8 Å [21]. This cage size is too small to accommodate bulky porphyrins such as *meso*-tetraphenylporphyrin (H_2TPP), which has a square-planar structure with molecular dimensions of approximately 15 × 15 $Å^2$. In contrast, medium- and large-pore molecular sieves can provide a more suitable microenvironment for suppressing back electron transfer and extending the lifetime of photo-generated ion pairs [22,23]. The interaction between the support and the active center can be minimized by employing supports with slightly larger pores, allowing spatial separation between the porphyrin center and the cavity wall.

Shen et al. [24] have immobilized cobalt tetrasulfophthalocyanine (CoTSPc) on structurally ordered mesoporous silicas (MCM-41, MCM-48, and SBA-15). Qiao et al. [19] incorporated TiO_2 nanoparticles and CdS quantum dots (QDs) into photoactive dendritic porphyrin-based mesoporous silica nanospheres (DPMSNs) to develop high-efficiency photocatalytic systems through precise nano-architectural control. Pirouzmand et al. [13] immobilized phthalocyanine complexes of cobalt, manganese, and iron within MCM-41 channels using microwave irradiation. Nur et al. [25] used poly(methyl methacrylate) (PMMA) and mesoporous molecular sieve Al-MCM-41 (Si/Al = 20) for the encapsulation of bulky iron(III) 5,10,15,20-tetra(4-pyridyl)porphyrin (Fe-TPyP). Xu et al. [26] reported the encapsulation of monomeric and aggregated tetrakis(*p*-sulfonatophenyl)porphyrin in an aluminosilicate mesostructure MCM-41 under different pH conditions. Farzaneh et al. [27] prepared cobalt complexes with ligands such as bipyridine and acetylacetonate, immobilized in Al-MCM-41, and applied them in the epoxidation of alkenes.

Luminescence-based optical oxygen sensors have been extensively developed, as the determination of molecular oxygen in both gas and liquid phases is critical across various fields, including analytical, medical, environmental, and industrial chemistry [23,28]. These sensors are based on the principle that oxygen is a powerful quencher of the luminescence intensity and lifetime of luminescent complexes. The optical properties of the luminescent complexes, along with the solubility and diffusion coefficient of oxygen in the matrix, are key parameters governing sensing performance [12,29,30].

Despite extensive studies on the immobilization of porphyrins and related macrocycles in mesoporous silica, comparatively limited attention has been devoted to systematically examining how the nature of the porphyrin center affects the structural and photophysical response under the same functionalized mesoporous environment. In particular, a direct comparison of free-base tetraphenylporphyrin (TPP) with zinc tetraphenylporphyrin (ZnTPP), cobalt tetraphenylporphyrin (CoTPP), and iron tetraphenylporphyrin (FeTPP) confined within the same amino-functionalized MCM-41 host provides a controlled framework for assessing differences associated with the central metal while retaining the same tetraphenylporphyrin ligand framework. 3-aminopropyltriethoxysilane (APTES) functionalization introduces primary amine groups onto the silica surface, thereby modifying the local chemical environment experienced by the porphyrin guests and providing chemically accessible sites for host–guest interactions, including hydrogen bonding and possible coordination-type interactions. The latter are considered cautiously in the present work, since the available characterization does not independently establish a specific metal–nitrogen coordination bond. The selection of Zn, Co, and Fe therefore enables a comparative assessment of metal-dependent photophysical behavior while minimizing structural variations associated with changes in the porphyrin ligand. Accordingly, the principal contribution of this study is the systematic comparison of the structural, optical, and excited-state behavior of TPP, ZnTPP, CoTPP, and FeTPP within the same amino-functionalized MCM-41 host, thereby establishing comparative structure–property relationships under a common confinement environment.

In this work, TPP, ZnTPP, CoTPP, and FeTPP were incorporated into amino-functionalized mesoporous silica MCM-41 using a straightforward impregnation method, and the resulting composites were systematically characterized to investigate their optical and physicochemical properties.

2. Materials and methods

Cetyltrimethylammonium bromide (CTAB, $C_{16}H_{33}N(CH_3)_3Br$) was purchased from Molychem, India, while tetramethylammonium hydroxide (TMAOH, $(CH_3)_4NOH$) and fumed silica were obtained from Kemphasol and Sigma-Aldrich, respectively. Mesoporous silica was synthesized following the procedure reported in previous work [31,32]. The molar composition of the initial mixture was SiO_2: 0.25 CTAB: 0.2 TMAOH: 40 H_2O. In a typical synthesis, 4.55 g of CTAB was dissolved in 33.3 mL of Milli-Q water under stirring for 45 min at room temperature (RT). Subsequently, 3.5 mL of TMAOH was added after complete dissolution of the surfactant, and the mixture was stirred for 1 h. After the addition of 3 g of fumed silica, the resulting gel was stirred at high speed for 3 h. The pH of the gel was initially 12.3 and slightly decreased to 12.2 after aging for 24 h at RT. The foam-like homogeneous gel was transferred into an autoclave and subjected to hydrothermal treatment at 135 °C for 48 h. The resulting solid product was filtered, washed with deionized water, and dried at 60 °C for 2–3 h. This treatment was considered a preliminary drying step to remove physically retained water rather than a complete dehydration or activation treatment; the residual water content was not quantitatively determined.

The dried as-synthesized MCM-41 was subsequently calcined in air at 550 °C for 6 h using a heating rate of 5 °C/min to remove the CTAB template and thermally activate the silica framework. After calcination, the material was allowed to cool to RT and stored under dry conditions before functionalization.

Free-base TPP, ZnTPP, CoTPP, and FeTPP were prepared according to a reported procedure [33]. Since amino groups can interact with porphyrin guests, the calcined MCM-41 was functionalized with APTES following a reported method [25]. Calcined MCM-41 (1.5 g) was dispersed in 100 mL of chloroform under stirring, after which 4.7 mL of APTES was added to the suspension. The mixture was stirred at RT for 10 h under an N_2 atmosphere. The functionalized solid was then separated by centrifugation and repeatedly washed with chloroform followed by dichloromethane to remove unreacted and physically adsorbed APTES. Finally, the product was dried under vacuum at RT for 4 h to obtain amino-functionalized MCM-41 (NH_2-Si-MCM-41).

For porphyrin incorporation, 2 mg of TPP, ZnTPP, CoTPP, or FeTPP was dissolved in 100 mL of $CHCl_3$, corresponding to a concentration of 0.02 mg/mL. NH_2-Si-MCM-41 (0.2 g) was added to each porphyrin solution, corresponding to a nominal porphyrin/support mass ratio of 1:100. The suspensions were stirred at RT for 24 h under an N_2 atmosphere to facilitate the interaction of the porphyrin molecules with the functionalized mesoporous silica and their potential incorporation into the pore channels. The solids were subsequently separated by centrifugation and washed three times with chloroform to remove loosely bound or externally deposited porphyrin. The resulting composites were finally

dried under vacuum at RT for 3 h. The actual porphyrin content retained in the final composites was not independently quantified by thermogravimetric or elemental analysis; therefore, the 1:100 ratio refers to the nominal porphyrin/support ratio used during impregnation rather than to the final porphyrin loading.

The structure and crystallinity of the porphyrin-incorporated NH_2-Si-MCM-41 samples were characterized using small- and wide-angle X-ray diffraction (XRD), performed on a Rigaku Miniflex diffractometer using Cu Kα radiation ($\lambda = 0.154$ nm). Nitrogen (N_2) adsorption measurements were performed using a Smart Sorb 90 system (Smart Instruments Pvt. Ltd., India) with a N_2/He gas mixture (70/30). Prior to analysis, the samples were degassed under vacuum at 80 °C for 4 h to remove physically adsorbed species. The Brunauer–Emmett–Teller (BET) method was used to estimate the specific surface area. Because no independent calibration-based uncertainty or statistically robust replicate dataset was available, a numerical accuracy was not assigned to the BET values; these values are therefore regarded as estimates of the accessible surface area within the limitations of the BET model and experimental conditions.

Ultraviolet–visible (UV–Vis) absorbance and photoluminescence (PL) measurements were carried out using PerkinElmer Lambda 950 and LS-55 instruments, respectively. Fourier transform infrared (FTIR) spectra were recorded using a Thermo Scientific Nicolet 6700 instrument, with KBr pellets used as the reference matrix and mixed with the samples. For the UV–Vis measurements, the free porphyrins in solution and the solid porphyrin/MCM-41 composites were characterized using different optical geometries, with the solid composites measured in diffuse-reflectance mode; accordingly, comparisons between the corresponding spectra were treated qualitatively. The steady-state PL spectra were recorded at an excitation wavelength of 418 nm. Time-resolved fluorescence measurements were performed using a time-correlated single-photon counting (TCSPC) system with excitation provided by a pulsed Nano-LED source (HORIBA Jobin Yvon) at 453 nm. Fluorescence was detected using a photomultiplier tube (PMT), with a time-to-amplitude converter (TAC) acquisition window of 100 ns. The instrument response function was determined using the time-domain method, and the fluorescence decay curves were fitted using IBH UK TCSPC analysis software.

3. Results and discussion

Porphyrins were incorporated into mesoporous silica MCM-41 using a wet chemical method. It is well known that free silanol groups are present on the surface of mesoporous silica. These silanol groups are reactive and can be functionalized with various agents [25].

Before the incorporation of porphyrins into MCM-41, mesoporous Si-MCM-41 was functionalized with APTES to introduce primary amine groups and modify the local chemical environment experienced by the porphyrin guests. The chemical reaction between mesoporous Si-MCM-41 and APTES is illustrated in Fig. 1a.

The crystal structure and bonding of the functionalized Si-MCM-41 sample were analyzed using XRD and FTIR techniques, as shown in Fig. 1b and c, respectively. A strong peak appearing at $2\theta = 1.78°$ corresponds to the (100) plane of the MCM-41 structure. It is found that, after silylation, the XRD pattern of the modified NH_2-MCM-41 is essentially identical to that of the original calcined MCM-41. The presence of a strong (100) reflection in the diffraction pattern of NH_2-Si-MCM-41 (Fig. 1b) indicates that the mesoporous structure of Si-MCM-41 remains intact after functionalization with APTES. However, a small shift of ~0.2° in the 2θ value toward higher angles is observed, indicating slight structural compression and a corresponding decrease in the interplanar spacing (d_{100}). This suggests that interaction between the

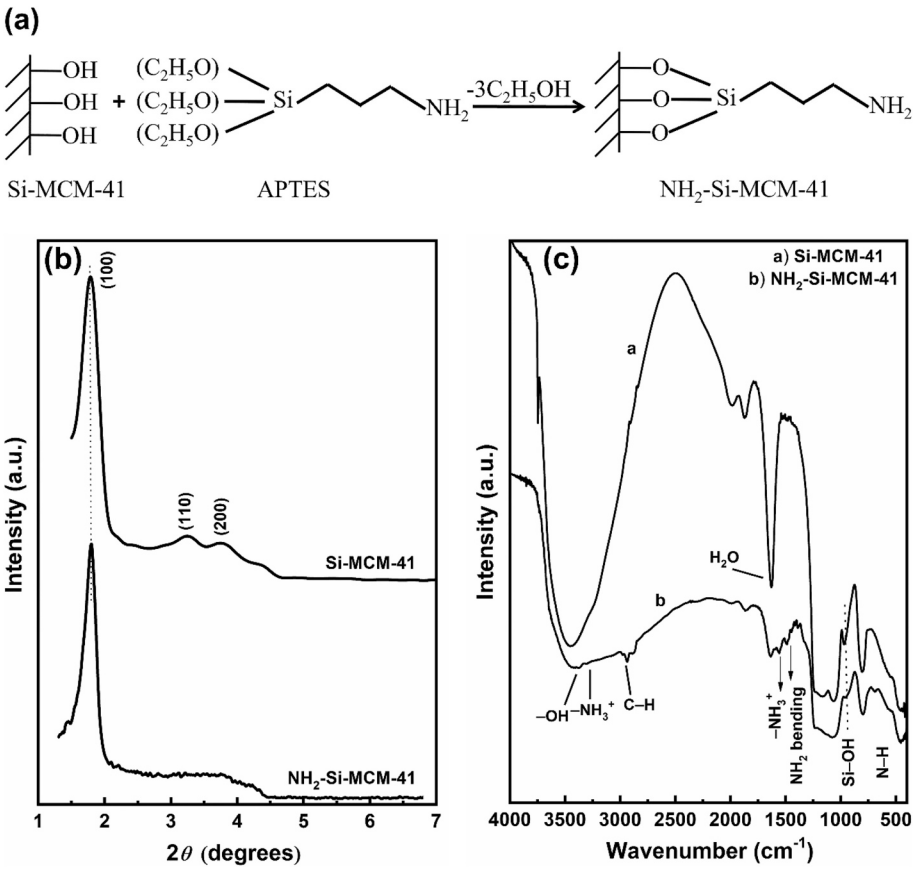


Fig. 1. (a) Schematic illustration of the functionalization reaction of Si-MCM-41, (b) XRD patterns and (c) FTIR spectra of pristine and functionalized Si-MCM-41 samples.

functionalizing molecules and the silica framework induces strain in the pore walls.

The bonding between Si-MCM-41 and the functionalizing molecule was investigated using FTIR spectroscopy (Fig. 1c).

The shift of the Si–OH vibration in Si-MCM-41 toward lower wavenumbers, from 964 to 947 cm^{-1}, indicates an interaction between $–NH_2$ groups and silanol groups through hydrogen bonding. The presence of N—H bending vibrations at 691 cm^{-1}, together with the appearance of a feature at 1503 cm^{-1} exclusively in the NH_2-Si-MCM-41 sample, supports modification of the silica surface after APTES functionalization [23–25]. As discussed below, the 1503 cm^{-1} feature is treated as unassigned because the available data do not support an unambiguous assignment to $–NH_2$ bending. The intensity of the peak at 3450 cm^{-1}, attributed to –OH stretching vibrations in Si-MCM-41, shifts to 3420 cm^{-1} and becomes broadened after functionalization with the silylating agent. The bands observed in the C—H stretching region of the Si-MCM-41 spectrum, including those near 2920 and 2850 cm^{-1}, require cautious interpretation because contributions from residual organic species cannot be excluded. Similarly, the feature in the region around 1630 cm^{-1} cannot by itself be regarded as unambiguous evidence for either the presence or complete removal of residual template. Accordingly, the FTIR data alone are not considered sufficient to demonstrate complete CTAB removal after calcination, and this limitation is taken into account when interpreting the subsequent functionalization and porphyrin-incorporation results.

Free-base tetraphenylporphyrin (TPP) and metalloporphyrins (M-TPP, where M = Zn, Co, and Fe) were incorporated into functionalized Si-MCM-41. For simplicity, the porphyrin-incorporated NH_2-Si-MCM-41 samples are hereafter denoted as TPP-M, ZnTPP-M, CoTPP-M, and FeTPP-M, corresponding to TPP-NH_2-Si-MCM-41, ZnTPP-NH_2-Si-MCM-41, CoTPP-NH_2-Si-MCM-41, and FeTPP-NH_2-Si-MCM-41, respectively. The resulting TPP-M, ZnTPP-M, CoTPP-M, and FeTPP-M composite materials were characterized using various techniques to evaluate their structural and optical properties. The molecular structure of metalloporphyrins is shown in Fig. 2, where M represents the central metal ion (Zn, Co, or Fe). The structural behavior of the final TPP-M, ZnTPP-M, CoTPP-M, and FeTPP-M composites was analyzed using XRD, as illustrated in Fig. 3.

No significant changes are observed in the diffraction patterns of functionalized MCM-41 after the incorporation of different porphyrins, except for a slight shift in 2θ, indicating that the mesoporous structure of MCM-41 remains intact [25–28]. The interplanar spacing d_{100} decreases by 6.3–7.0% for the porphyrin-incorporated NH_2-Si-MCM-41 composites relative to calcined Si-MCM-41, while functionalized MCM-41 exhibits a decrease of approximately 11%, as summarized in Table 1.

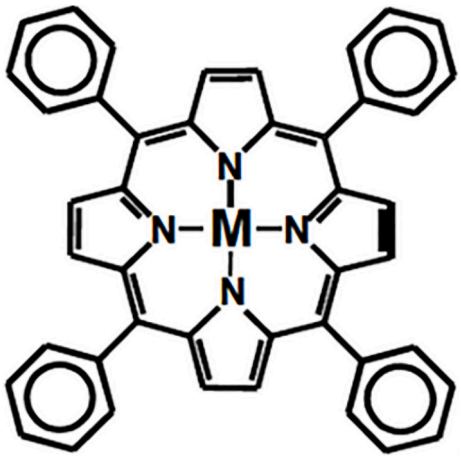


Fig. 2. Schematic illustration of the molecular structure of metallotetraphenylporphyrin (M-TPP), where M = Zn, Co, and Fe.

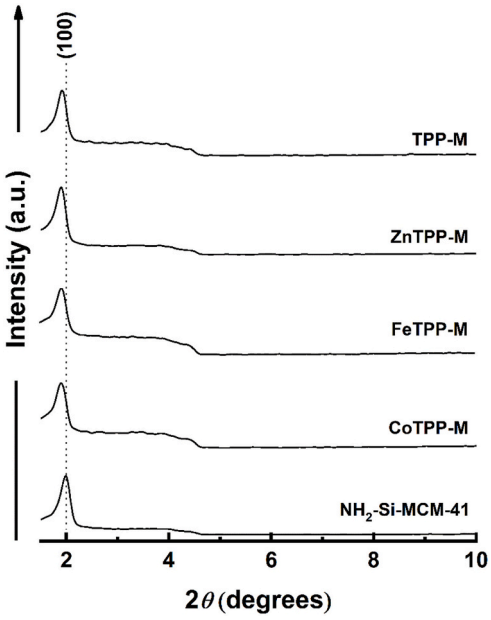


Fig. 3. Small-angle XRD patterns of NH_2-Si-MCM-41 and porphyrin-incorporated NH_2-Si-MCM-41 composite materials.

Table 1
Interplanar spacing (d_{100}), relative change in interplanar spacing (Δd_{100}), hexagonal lattice parameter (a_0), estimated pore size, and BET surface area of siliceous MCM-41, functionalized MCM-41, and porphyrin-incorporated NH_2-Si-MCM-41.

Sample	d_{100} (nm)	[a] Δd_{100} (%)	[b] a_0 (nm)	[c] Pore size (nm)	Surface area (m^2/g)
Si-MCM-41	4.95	–	5.71	4.71	947
NH_2-Si-MCM-41	4.41	10.9	5.09	4.09	679
TPP-M	4.60	7.0	5.31	4.31	67
ZnTPP-M	4.64	6.3	5.36	4.36	53
CoTPP-M	4.64	6.3	5.36	4.36	51
FeTPP-M	4.64	6.3	5.36	4.36	47

[a] Δd_{100} is calculated relative to Si-MCM-41.
[b] $a_0 = 2d_{100}/\sqrt{3}$.
[c] Pore size is estimated by subtracting 1 nm from a_0, assuming a pore wall thickness of ~1 nm [26].

The larger decrease in d_{100} for functionalized MCM-41 can be attributed to electrostatic interactions between the silylating molecules within the mesopores, leading to structural compression [25]. However, in the case of porphyrin-incorporated NH_2-Si-MCM-41, such electrostatic interactions are likely reduced.

The hexagonal lattice parameter (a_0) is calculated from d_{100}, obtained from the first peak in the XRD pattern using Bragg's law. The lattice parameter a_0 can be approximated as the sum of the internal pore diameter and pore wall thickness, allowing estimation of the pore size of mesoporous silica [26,34]. The values of a_0, pore size, and BET surface area for siliceous MCM-41, functionalized MCM-41, and porphyrin-incorporated NH_2-Si-MCM-41 are summarized in Table 1.

The apparent pore diameters reported in Table 1 should be interpreted with caution because they are estimated from the XRD-derived lattice parameter using an assumed pore wall thickness of ~1 nm. Consequently, these values represent approximate geometrical estimates rather than direct measurements of the pore diameter, particularly for functionalized and guest-loaded mesoporous materials. The small apparent increase of approximately 0.2–0.3 nm after porphyrin incorporation relative to NH_2-Si-MCM-41 should therefore not be interpreted as a physical expansion of the pore channels. Instead, the

substantial decrease in BET surface area provides more direct evidence of a marked reduction in the accessible surface following functionalization and porphyrin loading. The persistence of the characteristic (100) reflection after modification independently indicates preservation of the ordered MCM-41 framework.

The pore sizes of different MCM-41 samples were determined by subtracting an estimated pore wall thickness of 1 nm [26]. The hexagonal lattice parameter (a_0), pore size, and BET surface area of calcined Si-MCM-41 decrease after functionalization with 3-aminopropyltriethoxysilane (APTES), as summarized in Table 1. The pore size of calcined MCM-41 is estimated to be ~4.7 nm. However, upon the formation of a monolayer of the silylating agent during functionalization, the pore size decreases to ~4.0 nm.

The pore size of functionalized MCM-41 remains sufficiently large to accommodate the investigated porphyrin molecules, which have approximate dimensions of 15 × 15 $Å^2$ [35]. Following porphyrin incorporation, the calculated lattice parameter and apparent pore size values increase slightly, whereas the BET surface area decreases markedly. As discussed above, the small increase in the calculated pore size values is not interpreted as physical expansion of the mesoporous channels because these values depend on the simplified geometrical model and assumed pore wall thickness. The pronounced decrease in accessible surface area is instead consistent with substantial modification and possible partial occupation of the accessible pore environment following porphyrin incorporation.

The wide-angle XRD pattern of the ZnTPP-M sample (Fig. 4) does not show any characteristic peaks of ZnTPP, indicating that no distinct crystalline ZnTPP phase is detectable under the present measurement conditions. However, this observation does not exclude amorphous or highly dispersed ZnTPP species, including those potentially located on the external surface of MCM-41.

The XRD patterns of the different porphyrin-incorporated NH_2-Si-MCM-41 samples (not shown here) indicate that the ordered framework of functionalized MCM-41 is preserved after porphyrin incorporation. The diffuse reflectance UV–Vis spectra of TPP and different metalloporphyrins before and after incorporation into MCM-41 are shown in Fig. 5. The spectrum of functionalized MCM-41 does not exhibit any characteristic absorption peaks.

The spectral bands of the investigated porphyrins undergo significant changes upon incorporation, namely: (i) red shift of the Soret and Q bands, (ii) reduction in the intensity ratio of Soret to Q bands, and (iii) broadening of the Soret band. It has been reported that adsorption of organic molecules on oxide supports induces strong perturbations in spectral maxima and molar absorption coefficients [23–25]. The Soret band (B band) is red shifted by 16 and 24 nm for ZnTPP-M and CoTPP-M, respectively, whereas no significant shift is observed for TPP-M and FeTPP-M samples. Moreover, the Q band exhibits a red shift in all samples. These spectral changes should not be attributed exclusively to a single interaction mechanism. Changes in the local dielectric environment and host–guest interactions may contribute to the observed shifts, while porphyrin aggregation can also modify the Soret and Q bands through intermolecular excitonic coupling. Accordingly, the observed red shifts and Soret band broadening are interpreted as potentially arising from the combined effects of the local dielectric environment, host–guest interactions, and porphyrin aggregation rather than solely from interactions between the porphyrin π-electron system and the –NH_2-functionalized surface.

Accordingly, the observed UV–Vis spectral changes are interpreted as evidence that incorporation into functionalized MCM-41 modifies the electronic environment of the porphyrins, while the relative contributions of host–guest interactions, the local dielectric environment, and aggregation cannot be distinguished unambiguously from these measurements alone. The peak positions of the Soret and Q bands of TPP and metalloporphyrins (ZnTPP, CoTPP, and FeTPP) before and after

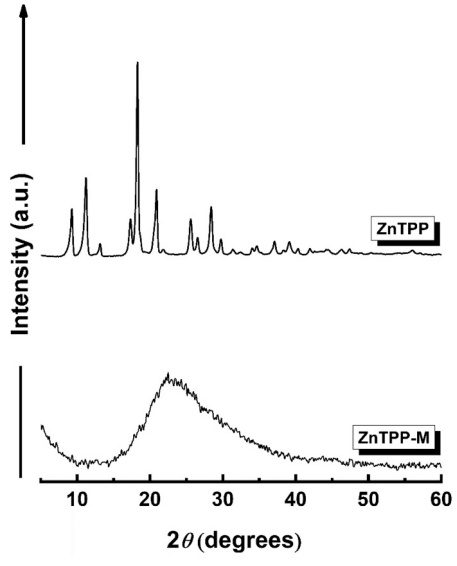


Fig. 4. Wide-angle XRD patterns of ZnTPP metalloporphyrin and ZnTPP-M composite samples.

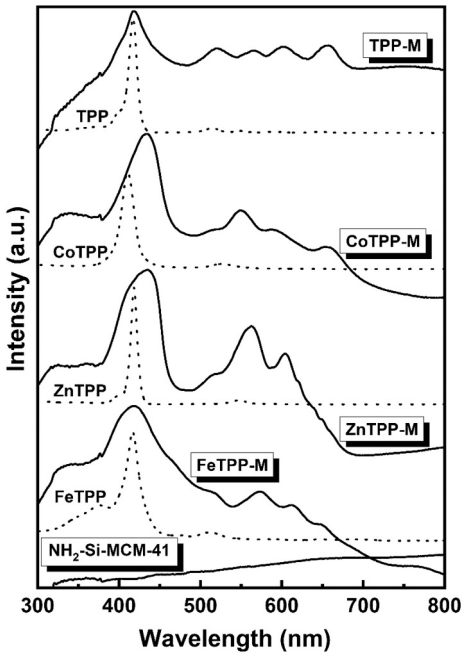


Fig. 5. Diffuse reflectance UV–Vis spectra of TPP and different metalloporphyrins before and after incorporation into functionalized MCM-41. The spectra of free TPP and metalloporphyrins are shown as dotted lines, while solid lines represent the corresponding porphyrin-incorporated functionalized MCM-41 composites.

Table 2
Peak positions of Soret and Q bands of TPP and metalloporphyrins (ZnTPP, CoTPP, and FeTPP) before and after incorporation into functionalized MCM-41.

Sample	Soret band (nm)	$\Delta\lambda$ (nm)	Q bands (nm)	$\Delta\lambda$ (nm)
TPP	417	0	513, 550, 591, 646	+6–13
TPP-M	417		519, 563, 601, 656	
ZnTPP	418	+16	510, 547, 585	+8–18
ZnTPP-M	434		518, 564, 603	
CoTPP	410	+24	527	+22
CoTPP-M	434		549, 590, 654	
FeTPP	417	0	543, 585	+26–31
FeTPP-M	417		574, 611, 648	

incorporation into functionalized MCM-41 are summarized in Table 2.

Because the free porphyrins in solution and the solid composites were characterized using different optical measurement geometries, the wavelength shifts reported in Table 2 should be interpreted qualitatively rather than as directly equivalent quantitative absorption measurements.

The fluorescence spectra of different porphyrins (TPP, ZnTPP, CoTPP, and FeTPP) before and after incorporation into functionalized MCM-41 are shown in Fig. 6. All spectra were recorded at an excitation wavelength of 418 nm. The fluorescence spectra of free porphyrins and those incorporated into functionalized MCM-41 are nearly identical, except for shifts in some of the emission bands (Table 3). Functionalized MCM-41 itself does not exhibit any emission (not shown here), indicating that the observed emission originates from the porphyrin species in the composite samples.

For clarity, F_1 and F_2 denote the first and second emission bands, respectively, as listed in Table 3. In the case of free-base tetraphenylporphyrin (TPP), a significant blue shift of 15 nm is observed in the F_1 emission band, whereas FeTPP exhibits a blue shift of 19 nm in the F_2 emission band after incorporation. Smaller shifts, including both blue and red shifts, are observed for the other emission bands. These changes are consistent with perturbation of the porphyrin excited-state environment following incorporation into functionalized MCM-41 [25,36,37]. However, the observed shifts cannot be assigned unambiguously to a single mechanism, because changes in the local dielectric environment, host–guest interactions, molecular packing, aggregation, and excited-state relaxation may contribute simultaneously. The emission peak positions of all porphyrins before and after incorporation into

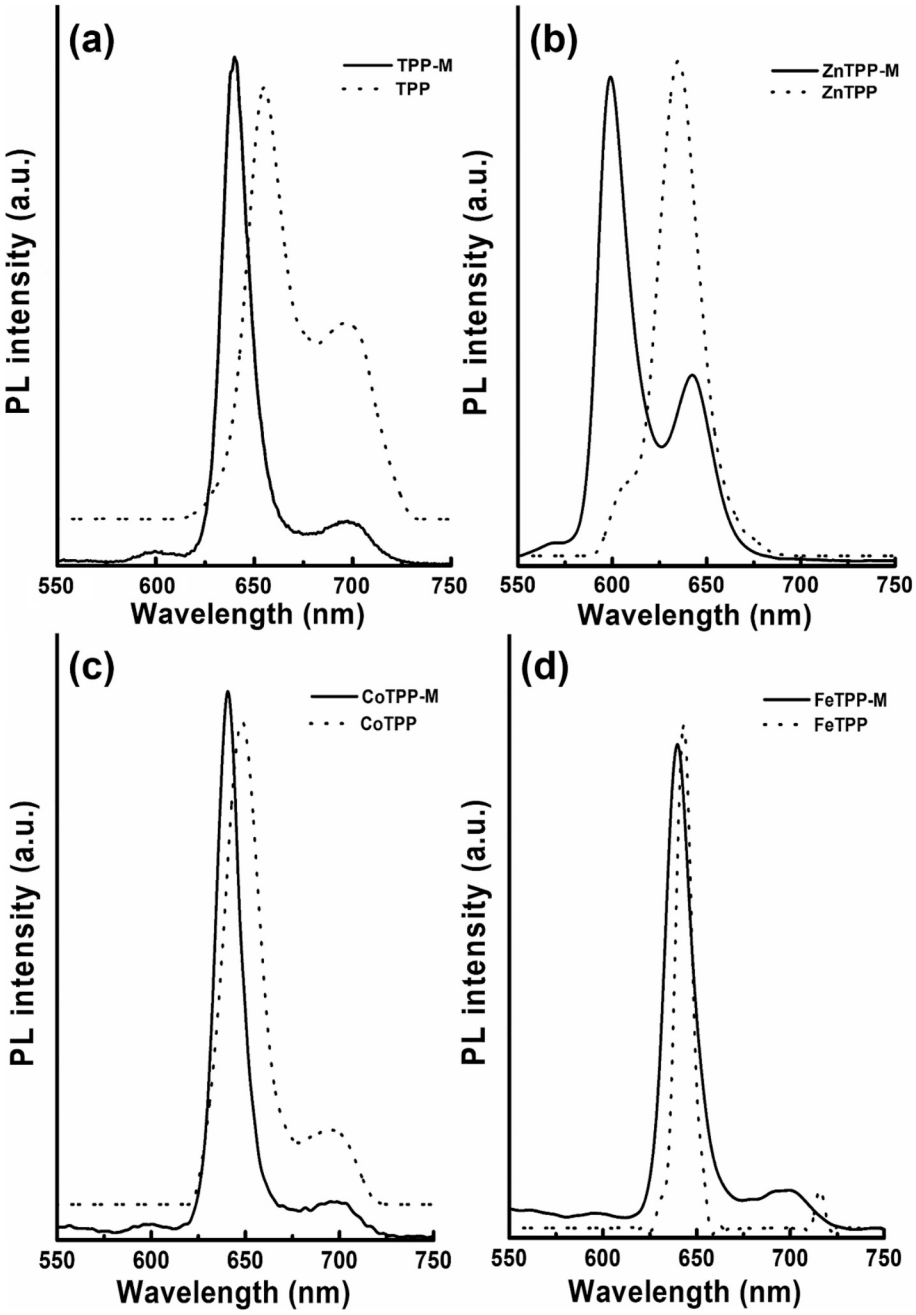


Fig. 6. PL spectra of (a) TPP, (b) ZnTPP, (c) CoTPP, and (d) FeTPP in solution and after incorporation into functionalized MCM-41. The spectra were recorded at an excitation wavelength of 418 nm. The dotted curves correspond to the emission of free porphyrins, whereas the continuous curves represent the emission of porphyrins incorporated into functionalized MCM-41.

Table 3
Emission peak positions (F_1 and F_2) and corresponding spectral shifts ($\Delta\lambda$) of free porphyrins and the corresponding porphyrin-containing functionalized MCM-41 samples. Negative values indicate a blue shift, whereas positive values indicate a red shift in the emission bands.

Sample	Emission band (nm)		$\Delta\lambda$ (nm)	
	F_1	F_2	F_1	F_2
TPP	655	697	−15	0
TPP-M	640	697		
ZnTPP	606	635	−7	+8
ZnTPP-M	599	643		
CoTPP	648	697	−8	0
CoTPP-M	640	697		
FeTPP	643	716	−3	−19
FeTPP-M	640	697		

functionalized MCM-41 are summarized in Table 3.

The apparent difference between the absorption and emission shifts can be understood by considering the different electronic processes probed by the two measurements. Absorption reflects transitions from the ground state to higher electronically excited states, whereas fluorescence occurs after excited-state vibrational and structural relaxation from the emissive excited state. Consequently, changes in the local dielectric environment, molecular packing, excitonic interactions, and excited-state relaxation can affect absorption and emission differently, and a bathochromic shift in absorption does not necessarily require an analogous shift in fluorescence. The observed emission shifts are therefore interpreted as arising from the combined effects of host-induced perturbation, molecular packing, and excited-state relaxation. Because no concentration- or loading-dependent spectroscopic studies were performed, the respective contributions of aggregation and coordination-related effects cannot be distinguished unambiguously from the present spectra.

The FTIR spectra provide evidence of changes in the chemical environment of the aminopropyl-functionalized silica following porphyrin incorporation. However, the present FTIR data do not independently establish the formation of a specific M–N coordination bond. Therefore, the observed spectral changes are interpreted as evidence of host–guest interactions involving the functionalized silica surface and porphyrin molecules [38], while definitive identification of metal–nitrogen coordination would require complementary techniques such as X-ray photoelectron spectroscopy (XPS), solid-state nuclear magnetic resonance (NMR), or X-ray absorption spectroscopy.

The bonding interactions between functionalized MCM-41 and the incorporated porphyrins were investigated using FTIR spectroscopy, as shown in Fig. 7. For comparison, the FTIR spectrum of functionalized MCM-41 is also presented. The assignments of selected IR peak positions for functionalized MCM-41 and porphyrin-incorporated functionalized MCM-41 samples are summarized in Table 4. The peaks at 3450 and 3064 cm^{-1} are attributed to the symmetric stretching vibrations of N—H and C—H groups, respectively [26]. A band near 1503 cm^{-1} is observed in functionalized MCM-41 but is absent after porphyrin incorporation. Because an unambiguous assignment of this feature to $–NH_2$ bending is not supported by the available data, it is treated as an unassigned spectral feature. Its disappearance after porphyrin incorporation is therefore interpreted cautiously as indicating a change in the local chemical environment rather than as direct evidence of a specific coordination mechanism. The peaks at 1237 and 1085 cm^{-1} are attributed to $Si–(CH_2)_3–NH_2$ and Si–O–Si stretching vibrations, respectively [26,30].

The changes in the FTIR spectra after porphyrin incorporation further indicate modification of the local chemical environment of the aminopropyl-functionalized silica. In particular, the bands associated with the aminopropyl groups exhibit changes in intensity following guest loading. The low-wavenumber region near 466 cm^{-1} is dominated by Si–O–Si framework vibrations, and the present FTIR data do not provide sufficient evidence to assign this feature to M–N coordination. Similarly, the feature near 952 cm^{-1} is primarily associated with surface silanol-related vibrations, whose intensity may be influenced by the local hydrogen-bonding environment, hydration state, and surface functionalization. Consequently, its increased intensity after porphyrin incorporation cannot by itself be regarded as evidence of metal–nitrogen coordination or porphyrin confinement. Overall, the FTIR results support modification of the host–guest chemical environment upon porphyrin incorporation but do not provide definitive evidence of a specific metal–nitrogen coordination bond.

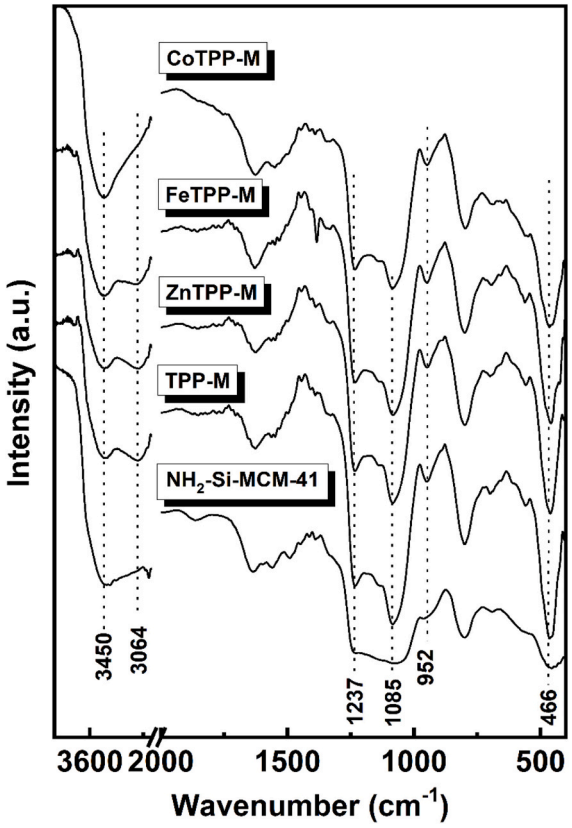


Fig. 7. FTIR spectra of functionalized MCM-41 and porphyrin-incorporated functionalized MCM-41 samples.

Table 4
Infrared vibration bands and their assignments for functionalized MCM-41 and porphyrin-incorporated functionalized MCM-41 samples (s: strong, w: weak).

Peak position (cm^{-1})	NH_2-Si-MCM-41	Porphyrin-incorporated NH_2-Si-MCM-41
3450	N–H stretching	N–H stretching
3064	C–H stretching (w)	C–H stretching (s)
1640	Si–OH stretching	Si–OH stretching
1551	N–H stretching	N–H stretching
1503	Unassigned feature	–
1237	$Si–(CH_2)_3–NH_2$ stretching (w)	$Si–(CH_2)_3–NH_2$ stretching (s)
1085	Si–O–Si stretching (w)	Si–O–Si stretching (s)
952	Si–OH bending (w)	Si–OH bending (s)
691	–NH bending	–NH bending
466	Si–O–Si (w)	Si–O–Si (s)

Fluorescence decay lifetime measurements were carried out to investigate the interaction between the silica host and the guest porphyrin molecules using a time-correlated single-photon counting (TCSPC) technique. The lifetime (τ) values were determined by fitting the experimental decay data using IBH UK TCSPC analysis software. The decay profiles were fitted with a multiexponential model, and the

quality of the fit was evaluated using the chi-square (χ^2) parameter, with values close to unity indicating satisfactory agreement between the fitted and experimental decay profiles.

The fluorescence decay components change after incorporation into functionalized MCM-41, as summarized in Table 5. The decay behavior of all porphyrins is multiexponential, indicating the presence of more than one fluorescence decay component. Changes in the individual lifetime components are observed after incorporation, and an additional decay component (τ_3) is required to describe ZnTPP-M, CoTPP-M, and FeTPP-M. Because the fractional amplitudes associated with the individual components are not available for the present dataset, amplitude-weighted average fluorescence lifetimes cannot be reliably calculated, and quantitative comparisons based on an overall average lifetime are therefore not made. Moreover, the individual lifetime components cannot be assigned unambiguously to specific structural or emitting species from the present decay data alone.

The changes in the individual fluorescence decay components and the appearance of additional components indicate that the porphyrins experience heterogeneous excited-state environments after incorporation into functionalized MCM-41. These changes may arise from differences in molecular packing, host–guest interactions, restricted molecular motion, and local microenvironmental heterogeneity. Although coordination between the porphyrin metal center and surface functional groups may contribute, the present lifetime data alone do not permit this mechanism to be distinguished unambiguously from aggregation or other non-radiative relaxation pathways.

The combined structural and spectroscopic results suggest that incorporation of porphyrins into amino-functionalized MCM-41 creates a heterogeneous local environment that differs from that experienced by the free molecules. The mesoporous environment can restrict molecular translational and rotational freedom and place the porphyrin macrocycles in proximity to the functionalized silica surface. Consequently, several processes may contribute to the observed optical response, including changes in the local dielectric environment, host–guest interactions, modified intermolecular packing, and restricted molecular motion. Upon optical excitation, these effects may influence the relative contributions of radiative and non-radiative relaxation pathways and thereby modify both the emission wavelength and the fluorescence decay behavior. The multiexponential decay observed for the composites is consistent with the presence of more than one excited-state environment. For metalloporphyrins, the central metal ion may additionally influence excited-state relaxation and intersystem-crossing pathways. However, the present measurements do not directly establish a specific electron-transfer pathway, energy-transfer mechanism, photocatalytic reaction pathway, or metal–nitrogen coordination mechanism. Therefore, charge- or energy-transfer processes are considered possible mechanisms that require further investigation using complementary time-resolved and surface-sensitive techniques.

The absence of the fractional amplitudes associated with the individual decay components represents a limitation of the present lifetime analysis and prevents calculation of reliable amplitude-weighted average fluorescence lifetimes. Accordingly, the TCSPC results are interpreted in terms of the individual decay components and the overall multiexponential behavior rather than through quantitative comparisons of average lifetimes.

Table 5
Fluorescence decay lifetime parameters obtained from multiexponential fitting of free porphyrins and the corresponding porphyrin-containing functionalized MCM-41 composites.

Sample	χ^2	τ_1 (ns)	τ_2 (ns)	τ_3 (ns)
TPP	1.30	4.3	17.3	–
TPP-M	1.38	4.2	16.8	–
ZnTPP	1.02	1.6	0.1	–
ZnTPP-M	1.07	1.9	0.2	7.4
CoTPP	1.48	21.2	8.3	–
CoTPP-M	1.30	8.5	2.6	0.2
FeTPP	1.17	5.0	20.0	–
FeTPP-M	1.28	3.8	8.5	0.5

The present study provides complementary structural, adsorption, vibrational, and optical characterization of the porphyrin/MCM-41 composites; however, some mechanistic aspects cannot be established unambiguously from the available measurements. In particular, quantitative porphyrin loading, concentration- or loading-dependent aggregation behavior, and direct identification of metal–nitrogen coordination were not independently determined. Furthermore, complete removal of the CTAB template and exclusive localization of the porphyrin molecules within the mesoporous channels could not be independently verified using the available characterization techniques. Electron microscopy measurements, including scanning electron microscopy (SEM) and transmission electron microscopy (TEM), were also not available for the present sample set; therefore, particle morphology and direct imaging of the mesostructural organization were not independently assessed. Techniques such as thermogravimetric analysis, elemental analysis, XPS, and concentration- or loading-dependent optical measurements would provide additional information in future studies. These measurements would help distinguish the relative contributions of confinement, aggregation, and specific host–guest interactions to the observed optical response.

4. Conclusions

In this study, TPP, ZnTPP, CoTPP, and FeTPP were incorporated into amino-functionalized MCM-41, and their structural and optical properties were comparatively investigated. Small-angle XRD confirmed that the characteristic ordered mesoporous structure of MCM-41 was retained after APTES functionalization and porphyrin incorporation. Nitrogen adsorption measurements showed a substantial reduction in accessible surface area after functionalization and guest loading, consistent with marked changes in the accessible pore environment. The apparent pore diameter values estimated from the XRD-derived lattice parameter using an assumed pore wall thickness were recognized as model-dependent and were therefore not interpreted as direct evidence of physical pore expansion or contraction.

The optical measurements demonstrated that incorporation into functionalized MCM-41 modifies the absorption and fluorescence characteristics of the porphyrins. The observed spectral changes are interpreted as potentially arising from the combined effects of changes in the local dielectric environment, host–guest interactions, and porphyrin aggregation. The different trends observed in absorption and emission are consistent with the distinct electronic processes probed by these measurements and with modifications of both the molecular environment and excited-state relaxation following incorporation. FTIR measurements further revealed changes in the vibrational environment of the aminopropyl-functionalized silica after porphyrin incorporation. However, the present FTIR data do not independently establish specific M–N coordination bonds, and the corresponding interactions were therefore interpreted cautiously. The multiexponential fluorescence decay profiles indicate the presence of multiple decay components and are consistent with heterogeneous excited-state environments within the composites.

Overall, the results demonstrate that amino-functionalized MCM-41 provides a mesoporous environment associated with modifications in the physicochemical and photophysical behavior of tetraphenylporphyrin derivatives and offers a useful platform for investigating environment-dependent optical behavior. Although the combined structural and spectroscopic results support porphyrin incorporation and modification of the mesoporous environment, the actual porphyrin loading, complete CTAB removal, and exclusive localization of the porphyrins within the mesoporous channels were not independently verified. Furthermore, the absence of fractional amplitudes in the fluorescence decay analysis prevents reliable quantitative comparisons of

average lifetimes. Quantitative determination of porphyrin loading, concentration- and loading-dependent spectroscopic studies, and complementary surface-sensitive characterization would be valuable for further elucidating the molecular origin of the observed host–guest interactions. Direct application-specific evaluation, including photocatalytic performance, reaction kinetics, quantum efficiency, active-species identification, stability, and recyclability, is reserved for future investigation.

CRediT authorship contribution statement

Prashant B. Lihitkar: Writing – original draft, Methodology, Investigation, Funding acquisition, Data curation, Conceptualization. **Sonali Kale:** Visualization, Validation, Methodology. **Rakesh A. Afre:** Writing – review & editing, Validation, Formal analysis. **Diego Pugliese:** Writing – review & editing, Validation, Supervision, Conceptualization.

Funding

This research did not receive any specific grant from funding agencies in the public, commercial, or non-profit sectors.

Declaration of competing interest

The authors declare that they have no known competing financial interests or personal relationships that could have appeared to influence the work reported in this paper.

Acknowledgements

P. B. Lihitkar would like to thank Dr. A. S. Kumbhar (Department of Chemistry, SPPU, Pune) for providing the facility for fluorescence lifetime measurements. He also thanks Prof. S. K. Kulkarni for his guidance and constant support during this work and acknowledges Dr. R. H. Naik for providing metalloporphyrins used in this study.

Data availability

Data will be made available on request.

References

[1] T. Li, Y.-T. Chen, X.-B. Zhang, R.-R. Du, L.-N. Ma, Y.-Q. Lan, Asymmetric heterogeneous catalysis using crystalline porous materials, Chem. Soc. Rev. 54 (2025) 5912–5960, https://doi.org/10.1039/D4CS00538D.
[2] C.H. Mak, X. Han, M. Du, J.-J. Kai, K.F. Tsang, G. Jia, K.-C. Cheng, H.-H. Shen, H.-Y. Hsu, Heterogenization of homogeneous photocatalysts utilizing synthetic and natural support materials, J. Mater. Chem. A 9 (2021) 4454–4504, https://doi.org/10.1039/D0TA08334H.
[3] X. Zhang, F. Zhang, K.-Y. Chan, Synthesis of titania–silica mixed oxide mesoporous materials, characterization and photocatalytic properties, Appl. Catal., A 284 (2005) 193–198, https://doi.org/10.1016/j.apcata.2005.01.037.
[4] X. Wang, W. Lian, X. Fu, J.-M. Basset, F. Lefebvre, Structure, preparation and photocatalytic activity of titanium oxides on MCM-41 surface, J. Catal. 238 (2006) 13–20, https://doi.org/10.1016/j.jcat.2005.11.027.
[5] A. Tuel, L.G. Hubert-Pfalzgraf, Nanometric monodispersed titanium oxide particles on mesoporous silica: synthesis, characterization, and catalytic activity in oxidation reactions in the liquid phase, J. Catal. 217 (2003) 343–353, https://doi.org/10.1016/S0021-9517(03)00078-2.
[6] M. Anpo, N. Aikawa, Y. Hubokawa, M. Che, C. Louis, E. Giamello, Photoluminescence and photocatalytic activity of highly dispersed titanium oxide anchored onto porous Vycor glass, J. Phys. Chem. 89 (1985) 5017–5021, https://doi.org/10.1021/j100269a025.
[7] J.F. Díaz, K.J. Balkus, Enzyme immobilization in MCM-41 molecular sieve, J. Mol. Catal. B Enzym. 2 (1996) 115–126, https://doi.org/10.1016/S1381-1177(96)00017-3.
[8] P.H. Pandya, R.V. Jasra, B.L. Newalkar, P.N. Bhatt, Studies on the activity and stability of immobilized α-amylase in ordered mesoporous silicas, Microporous Mesoporous Mater. 77 (2005) 67–77, https://doi.org/10.1016/j.micromeso.2004.08.018.
[9] F. Farzaneh, J. Taghavi, R. Malakooti, M. Ghandi, Immobilized vitamin B_{12} within nanoreactors of MCM-41 as selective catalyst for oxidation of organic substrates, J. Mol. Catal. A Chem. 244 (2006) 252–257, https://doi.org/10.1016/j.molcata.2005.08.058.
[10] M.D. Alba, Z. Luan, J. Klinowski, Titanosilicate mesoporous molecular sieve MCM-41: synthesis and characterization, J. Phys. Chem. 100 (1996) 2178–2182, https://doi.org/10.1021/jp9515895.
[11] J.M. Kisler, A. Dähler, G.W. Stevens, A.J. O'Connor, Separation of biological molecules using mesoporous molecular sieves, Microporous Mesoporous Mater. 44–45 (2001) 769–774, https://doi.org/10.1016/S1387-1811(01)00259-1.
[12] S. Chongdar, S. Bhattacharjee, P. Bhanja, A. Bhaumik, Porous organic–inorganic hybrid materials for catalysis, energy and environmental applications, Chem. Commun. 58 (2022) 3429–3460, https://doi.org/10.1039/D1CC06340E.
[13] M. Pirouzmand, M.M. Amini, N. Safari, Microwave-assisted immobilization of metallophthalocyanines in mesoporous channels of MCM-41, J. Porphyrins Phthalocyanines 11 (2007) 118–124, https://doi.org/10.1142/S1088424607000151.
[14] S.R.D. Gamelas, J.P.C. Tomé, A.C. Tomé, L.M.O. Lourenço, Porphyrin-containing materials for photodegradation of organic pollutants in wastewaters: a review, Catal. Sci. Technol. 14 (2024) 2352–2389, https://doi.org/10.1039/D4CY00092G.
[15] F. Cucinotta, B.P. Jarman, C. Caplan, S.J. Cooper, H.J. Riggs, J. Martinelli, K. Djanashvili, E. La Mazza, F. Puntoriero, Light-harvesting antennae using the host–guest chemistry of mesoporous organosilica, ChemPhotoChem 2 (2018) 196–206, https://doi.org/10.1002/cptc.201700144.
[16] J. Szymczak, M. Kryjewski, Porphyrins and phthalocyanines on solid-state mesoporous matrices as catalysts in oxidation reactions, Materials 15 (2022) 2532, https://doi.org/10.3390/ma15072532.
[17] A. Charisiadis, V. Nikolaou, E. Nikoloudakis, K. Ladomenou, G. Charalambidis, A. G. Coutsolelos, Metalloporphyrins in bio-inspired photocatalytic conversions, Chem. Commun. 61 (2025) 4630–4646, https://doi.org/10.1039/d4cc06655c.
[18] S. Kumari, A. Ramesh, B. Das, S. Ray, Zeolite-Y encapsulated cobalt(II) Schiff-base complexes for photocatalytic dye-degradation and upcycling CO_2, Inorg. Chem. Front. 8 (2021) 1553–1566, https://doi.org/10.1039/D0QI01190H.
[19] X. Qiao, T. Zhang, H. Zhang, Z. Xiong, R. Wang, Z. Zhang, S. Qiu, Incorporation of ultrafine TiO_2/CdS heterojunctions in dendritic porphyrins mesoporous silica nanospheres for efficient photocatalytic oxidation of styrene, J. Colloid Interface Sci. 691 (2025) 137365, https://doi.org/10.1016/j.jcis.2025.137365.
[20] M. Ikai, Y. Maegawa, Y. Goto, T. Tani, S. Inagaki, Synthesis of visible-light-absorptive and hole-transporting periodic mesoporous organosilica thin films for organic solar cells, J. Mater. Chem. A 2 (2014) 11857–11865, https://doi.org/10.1039/C4TA01136H.
[21] T. Tatsumi, M. Nakamura, S. Negishi, H. Tominaga, Shape-selective oxidation of alkanes with H_2O_2 catalysed by titanosilicate, J. Chem. Soc. Chem. Commun. (1990) 476–477, https://doi.org/10.1039/C39900000476.
[22] J.S. Reddy, R. Kumar, Synthesis, characterization, and catalytic properties of a titanium silicate, TS-2, with MEL structure, J. Catal. 130 (1991) 440–446, https://doi.org/10.1016/0021-9517(91)90126-O.
[23] B.T. Holland, C. Walkup, A. Stein, Encapsulation, stabilization, and catalytic properties of flexible metal porphyrin complexes in MCM-41 with minimal electronic perturbation by the environment, J. Phys. Chem. B 102 (1998) 4301–4309, https://doi.org/10.1021/jp9812738.
[24] C. Shen, Y. Wen, Z. Shen, J. Wu, W. Liu, Facile, green encapsulation of cobalt tetrasulfophthalocyanine monomers in mesoporous silicas for the degradative hydrogen peroxide oxidation of azo dyes, J. Hazard. Mater. 193 (2011) 209–215, https://doi.org/10.1016/j.jhazmat.2011.07.046.
[25] H. Nur, H. Hamid, S. Endud, H. Hamdan, Z. Ramli, Iron-porphyrin encapsulated in poly(methacrylic acid) and mesoporous Al-MCM-41 as catalysts in the oxidation of benzene to phenol, Mater. Chem. Phys. 96 (2006) 337–342, https://doi.org/10.1016/j.matchemphys.2005.07.023.
[26] W. Xu, H. Guo, D.L. Akins, Aggregation of tetrakis(*p*-sulfonatophenyl)porphyrin within modified mesoporous MCM-41, J. Phys. Chem. B 105 (2001) 1543–1546, https://doi.org/10.1021/jp003863n.
[27] F. Farzaneh, M. Jalalian, L. Tayebi, Epoxidation of alkenes with molecular oxygen catalyzed by immobilized $Co(acac)_2$ and $Co(bpy)_2Cl_2$ complexes within nanoreactors of Al-MCM-41, J. Chem. 9 (2012) 2205–2212, https://doi.org/10.1155/2012/896327.
[28] Z. Luan, E.M. Maes, P.A.W. van der Heide, D. Zhao, R.S. Czernuszewicz, L. Kevan, Incorporation of titanium into mesoporous silica sieve SBA-15, Chem. Mater. 11 (1999) 3680–3686, https://doi.org/10.1021/cm9905141.
[29] J.-W. Seng, L. Tong, X.-Q. Peng, W.-Y. Chang, W. Xie, Y.-H. Wang, J.-F. Zheng, Y. Shao, J.-Z. Chen, S. Jin, X.-S. Zhou, Influence of a coordinated metal center on charge transport through a series of porphyrin molecular junctions, J. Phys. Chem. C 126 (2022) 1168–1175, https://doi.org/10.1021/acs.jpcc.1c08667.
[30] S. Ghosh, A. Modak, A. Samanta, K. Kole, S. Jana, Recent progress in materials development for CO_2 conversion: issues and challenges, Mater. Adv. 2 (2021) 3161–3187, https://doi.org/10.1039/D1MA00107H.
[31] P.B. Lihitkar, M.K. Abyaneh, V. Samuel, R. Pasricha, S.W. Gosavi, S.K. Kulkarni, Titania nanoparticles synthesis in mesoporous molecular sieve MCM-41, J. Colloid Interface Sci. 314 (2007) 310–316, https://doi.org/10.1016/j.jcis.2007.05.069.
[32] P.B. Lihitkar, S. Violet, M. Shirolkar, J. Singh, O.N. Srivastava, R.H. Naik, S. K. Kulkarni, Confinement of zinc oxide nanoparticles in ordered mesoporous silica MCM-41, Mater. Chem. Phys. 133 (2012) 850–856, https://doi.org/10.1016/j.matchemphys.2012.01.106.
[33] R. Naik, P. Joshi, S.P. Kaiwar, R.K. Deshpande, Facile synthesis of *meso*-substituted dipyrromethanes and porphyrins using cation exchange resins, Tetrahedron 59 (2003) 2207–2213, https://doi.org/10.1016/S0040-4020(03)00245-X.

[34] P.A. Leermakers, H.T. Thomas, L.D. Weis, F.C. James, Spectra and photochemistry of molecules adsorbed on silica gel. IV, J. Am. Chem. Soc. 88 (1966) 5075–5083, https://doi.org/10.1021/ja00974a006.
[35] M.J. Hamor, T.A. Hamor, J.L. Hoard, The structure of crystalline tetraphenylporphine. The stereochemical nature of the porphine skeleton, J. Am. Chem. Soc. 86 (1964) 1938–1942, https://doi.org/10.1021/ja01064a008.
[36] S.M.S. Sajadi, S. Khoee, The simultaneous role of porphyrins' H- and J- aggregates and host–guest chemistry on the fabrication of reversible Dextran-PMMA polymersome, Sci. Rep. 11 (2021) 2832, https://doi.org/10.1038/s41598-021-82256-7.
[37] H. Sun, S. Lu, Y. Qi, J. Wu, T. Liu, J.-S. Qin, H. Rao, Metalloporphyrin/phthalocyanine catalysts for electrocatalytic nitrogen fixation, Adv. Sci. 12 (2025) e09323, https://doi.org/10.1002/advs.202509323.
[38] P.P. Martin, N. Fellenz, M. Calero, M.A. Martín-Lara, Fixed-bed column performance of amino-functionalized MCM-41 mesoporous silica for Cr(VI) removal: optimization of operating conditions and regeneration studies, Next Mater. 11 (2026) 101817, https://doi.org/10.1016/j.nxmate.2026.101817.